Characterization of the three-dimensional turbulent boundary layer in a concentric annulus with a rotating inner cylinder

Seo Yoon Jung and Hyung Jin Sung[a)]
Department of Mechanical Engineering, Korea Advanced Institute of Science and Technology, 373-1, Guseong-dong Yuseong-gu, Daejeon, 305-701, Korea

(Received 19 January 2006; accepted 10 October 2006; published online 20 November 2006)

Direct numerical simulations of fluid flow through a concentric annulus with a rotating inner wall were performed at $\mathrm{Re}_{Dh}=8900$. To elucidate the modifications of the near-wall turbulent structure induced by rotation of the inner wall, we compared data obtained at rotation rates of $N=0.0$ and 0.429 for a system with a radius ratio (R^*) of 0.5. Conditional quadrant/octant analysis and probability density functions of the velocity fluctuations revealed distinctive features of the three-dimensional turbulent boundary layer (3DTBL) in the concentric annulus with a rotating inner wall. Coherent structures near the inner wall were identified by a λ_2-based eduction scheme to give the detailed information on the activated near-wall turbulent structures. The ensemble-averaging of the educed coherent vortices showed that enhanced ejections near the vortices were primarily responsible for the augmented turbulent structures. The alteration of the turbulent structures was attributed to the centrifugal force arising from rotation of the inner wall. The assumption of Littell and Eaton on the cause of the altered turbulent structures in 3DTBLs was invalid in the present study. Taken together, the present results showed that the 3DTBL in a rotating concentric annulus has features different from those observed in other types of 3DTBL due to the transverse curvature. © *2006 American Institute of Physics*. [DOI: 10.1063/1.2391387]

I. INTRODUCTION

A three-dimensional turbulent boundary layer (3DTBL) is a boundary layer in which the mean flow direction changes with distance from the wall. Many engineering flows are three-dimensional in nature; for example, those on swept wings of aircraft, rotating propeller hubs, rotating disks, inside curved ducts, and submarine hulls. Thus, understanding the behavior of 3DTBLs is of great practical relevance. The turbulent flow of a fluid moving through a concentric annulus with a rotating inner wall can also be considered as a 3DTBL. Large-eddy simulation (LES) studies of rotating annular flows have shown that the shear stress angle lags behind the strain angle in such flows,[1] a feature observed in many previous studies of 3DTBLs. Therefore, elucidating the behavior of turbulent rotating flows in concentric annuli should provide insight into the general problem of 3DTBLs.

In general, 3DTBLs can be classified as either pressure- or shear-driven flows. Pressure-driven 3DTBLs are boundary layers that are perturbed by a mean spanwise pressure gradient. There have been many experimental and numerical studies on pressure-driven 3DTBLs.[2–9] In shear-driven 3DTBLs, by contrast, a transverse shear is generated by a moving wall. Turbulent rotating flow in a concentric annulus falls into this category. Several experimental and numerical investigations have examined shear-driven 3DTBLs.[10–16] In studies of the longitudinal flow along a spinning cylinder, Lohmann[10] found that the transverse velocity boundary layer grows at a rate approximately proportional to $x^{0.5}$, where x is the downstream distance from the beginning of the moving section, and that the stress angle lags behind the mean velocity gradient angle. Littell and Eaton[11] examined the 3DTBL created by a free rotating disk. To investigate the characteristics of the near-wall structures, they measured the conditionally averaged velocities. Their results showed asymmetric patterns in the conditionally averaged quantities, which they attributed to the modification of the shear-stress-producing structures by cross-flow. Specifically, they hypothesized that cross-flow reduces the ability of the streamwise vortices of one sign to produce strong ejections, while weakening the ability of those of the other sign to produce strong sweeps. However, in a study of a similar rotating disk flow system, Kang *et al.*[13] concluded that the asymmetries in the conditional averages are caused by non-Reynolds-stress-producing events rather than modification of the shear-stress-producing structures by cross-flow. This issue was further examined in recent LES and direct numerical simulation (DNS) calculations[15,16] of rotating disk flows, which gave results supporting the conclusions of Littell and Eaton.[11] Kannepalli and Piomelli[14] carried out a LES study of a spatially developing shear-driven 3DTBL generated by moving a section of the wall in the transverse direction. They observed disruption of the outer-layer vortical structures in addition to the salient features of 3DTBLs in previous findings.

A well-known feature of both pressure- and shear-driven flows is that the shear stress angle γ_τ is usually smaller than the mean velocity gradient angle γ_g. This lack of alignment between the Reynolds stress and the mean shear also exists in stationary 3DTBLs such as the flow in a rotating concentric annulus considered in the present study. The stress/strain misalignment cannot be captured by any turbulence model

a)Author to whom correspondence should be addressed. Electronic mail: hjsung@kaist.ac.kr

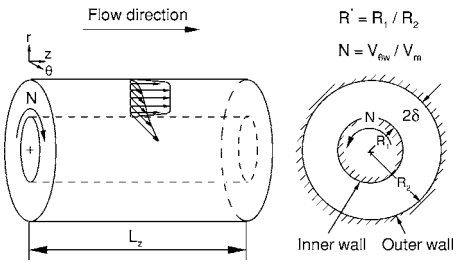

FIG. 1. Schematic diagram of the computational domain.

that assumes an isotropic eddy viscosity. To overcome this difficulty, one must understand which terms in the Reynolds-stress transport equation are responsible for the misalignment between the stress and strain.

Another consistent trend in 3DTBLs is that throughout the entire 3DTBL, the structure parameter (a_1; defined as the ratio of the shear stresses to twice the turbulent kinetic energy) is lower than that of the initial two-dimensional state. As pointed out by Schwarz and Bradshaw,[6] this alteration implies that the turbulence becomes less efficient in extracting energy from the mean flow after cross-flow has appeared. Bradshaw and Pontikos[2] hypothesized that turbulent eddies formed in a two-dimensional boundary layer are tilted out of their preferred orientation by the mean three-dimensionality. On the other hand, Littell and Eaton[11] suggested that the modification of a_1 is due in part to a modification of near-wall structures rather than being purely a disequilibrium effect. In support of their theory, they observed strong asymmetry in the near-wall vortical structures, which leads to a reduction in turbulent energy near the wall. Despite the many studies on 3DTBLs, many open questions remain regarding the changes of a_1.

In the present work, we simulated a turbulent rotating flow in a concentric annulus using DNS in order to elucidate the effect on the near-wall structure of rotating the inner wall. The system studied is similar to that examined in a recent LES study.[1] However, that previous study did not consider the detailed flow structures, whereas in the present study we devote particular attention to the changes in the near-wall turbulent structure induced by rotation of the inner wall. A schematic diagram of the computational domain is shown in Fig. 1. Two rotation rates, $N=0.0$ and 0.429, were selected and the radius ratio (R^*) was 0.5. The Reynolds number based on the bulk velocity (V_m) and the hydraulic diameter ($D_h=4\delta$) was 8900. Various conditional averaging techniques are employed to analyze the near-wall turbulent structures. Four characteristic flow angles are introduced to remove the bulk rotation effects. To observe asymmetries in the turbulent structures, conditional quadrant/octant analysis for the Reynolds shear stress and probability density functions (pdfs) of the velocity fluctuations are employed. Finally, coherent structures near the inner wall are identified by means of the λ_2 vortex criterion in order to shed further light on the transverse curvature effects on activated near-wall turbulent structures in rotating concentric annuli.

II. NUMERICAL METHODS

The numerical conditions used in the present work were similar to those of Chung and Sung,[1] except that no model was employed and finer streamwise and azimuthal grid resolutions were used. Two rotation rates ($N=0.0$ and 0.429) were selected to compare the 3DTBL in a rotating annulus with the two-dimensional flow in the corresponding nonrotating annulus. The computational domain was one-quarter of the full cross section of the concentric annular pipe. The computational length in the streamwise direction was $L_z=18\delta$ in all cases. The adequacy of the above computational domain was confirmed by calculating two-point correlations of the fluctuating streamwise velocities and temperature in the streamwise and azimuthal directions for all cases. The time step was $0.03\delta/V_m$ and the total averaging time was $750\delta/V_m$ in all cases. In the wall-normal direction, grid points were clustered according to a hyperbolic tangent distribution. The number of grid points in the r, θ, and z directions was $65\times256\times256$, respectively. The mesh resolutions were $\Delta z^+=10.55$ and 11.95, $\Delta r^+_{\min}=0.25$ and 0.28, $\Delta r^+_{\max}=12.89$ and 14.53, $R_1\Delta\theta^+=1.84$ and 2.09, and $R_2\Delta\theta^+=3.68$ and 4.17 for the $N=0.0$ and 0.429 systems, respectively. Periodic boundary conditions were applied in the axial and circumferential directions for the velocity components, and a no-slip boundary condition was imposed at the solid walls.

The governing equations were integrated in time using the fractional step method with the implicit velocity decoupling procedure proposed by Kim *et al.*[17] Under this approach, the terms are first discretized in time using the Crank-Nicolson method, and then the coupled velocity components in the convection terms are decoupled using the implicit velocity decoupling procedure. The decoupled velocity components are then solved without iteration. Because the implicit decoupling procedure relieves the Courant-Friedrichs-Lewy restriction, the computation time is reduced significantly. In the preliminary calculation for the present flow configuration, the comparison between the iterative numerical scheme and the present one was made. Usually, three or four iterations were needed to get a converged solution with the coupled velocity components. The computational time of the iterative scheme was 1.6–1.9 times larger than that of Kim *et al.*[17] The overall accuracy in time is second-order. All the terms are resolved using a second-order central difference scheme in space with a staggered mesh. Details regarding the numerical algorithm can be found in the paper of Kim *et al.*[17]

III. RESULTS AND DISCUSSION

A. Mean flow properties and second-order statistics

Before proceeding further, it is important to first establish the reliability and accuracy of the present numerical simulations. Table I lists the mean flow parameters for the two N values considered here. The average skin friction coefficient ($C_f=R_1/(R_1+R_2)C_{f,\text{inner}}+R_2/(R_1+R_2)C_{f,\text{outer}}$) based on the friction velocity $\{Q_\tau=[(\tau_z^2+\tau_\theta^2)^{0.5}/\rho]^{0.5}\}$ for $N=0.0$ (see Table I) is similar to that calculated by Chung *et al.*[18]

TABLE I. Mean flow parameters

N	0.0	0.429
$\mathrm{Ta}=[(R_2-R_1)/R_1]^{0.5}V_{\theta w}(R_2-R_1)/\nu$ (Present)	0.00	1909.05
$\mathrm{Re}_{\tau,\mathrm{inner}}=Q_{\tau,\mathrm{inner}}\delta/\nu$ (Present)	150.72	173.47
$\mathrm{Re}_{\tau,\mathrm{outer}}=\mathrm{Q}_{\tau,\mathrm{outer}}\delta/\nu$ (Present)	142.79	145.60
$C_{f,\mathrm{inner}}$ (Present)	0.009 18	0.012 16
$C_{f,\mathrm{outer}}$ (Present)	0.008 24	0.008 56
C_f (Present)	0.008 55	0.009 76
C_f (Ref. 18) $N=0.0$	0.008 80	⋯
C_f (Ref. 1) $N=0.429$	⋯	0.009 86
C_f (Ref. 19) $N=0.429$	⋯	0.010 48

Here, $C_{f,\mathrm{inner}}=(\tau^2_{z,\mathrm{inner}}+\tau^2_{\theta,\mathrm{inner}})^{0.5}/(0.5\rho V_m^2)$ and $C_{f,\mathrm{outer}}=(\tau^2_{z,\mathrm{outer}}+\tau^2_{\theta,\mathrm{outer}})^{0.5}/(0.5\rho V_m^2)$. The C_f value for $N=0.429$ is larger than that for $N=0.0$, while being consistent with the results of previous experimental and numerical studies.[18,19]

Comparison of the mean streamwise velocity distributions calculated in the present study with experimental data[19] for $N=0.429$ [Fig. 2(a)] shows that, except for slight deviations in the center region and near the outer wall, the numerical and experimental results are in satisfactory agreement. Here, y_1 is the distance from the inner wall. It is interesting to note that integration of the experimentally determined profiles in the radial direction does not yield a value of unity. The integrated value using the Riemann sums of the experimental data is 1.064. This stands in contrast to the numerical profiles, which yield values of 1.0 upon integration. After rescaling of the experimental data by a normalization process[18] to give an integral in the radial direction of unity, the numerical prediction was in good agreement with the experimental data. Note that, as pointed out by Nouri and Whitelaw,[19] the profiles become flatter and less skewed with increasing N. To further compare our numerical results with previous simulation and experimental findings, Fig. 2(b) depicts the calculated mean azimuthal velocities normalized by the rotational speed of the inner wall along with the corresponding LES data of Chung and Sung[1] and experimental data of Nouri and Whitelaw.[19] Compared with the LES results, the present DNS data are in quantitatively better agreement with the experimental data.

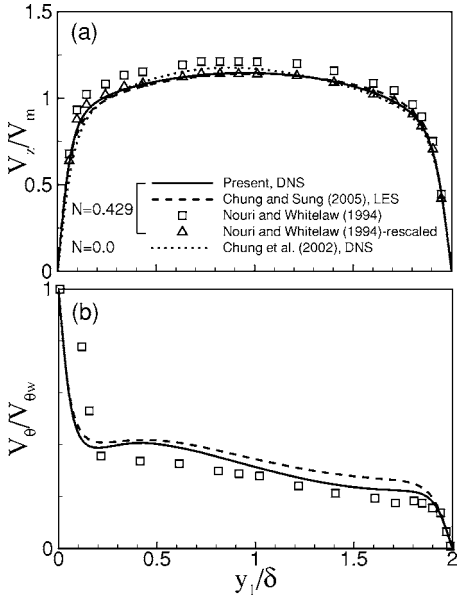

FIG. 2. Distributions of mean streamwise velocity and azimuthal velocity.

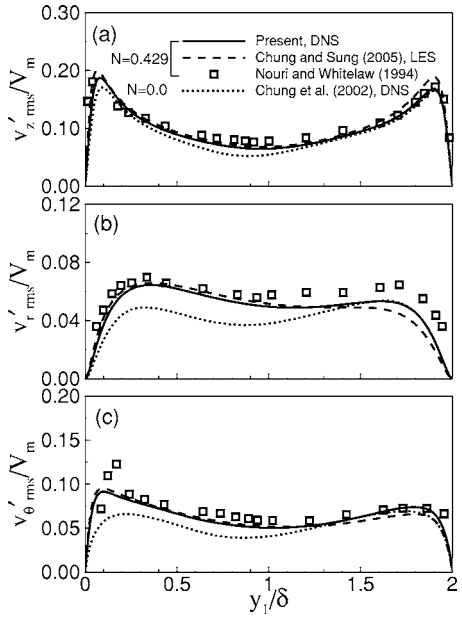

FIG. 3. Root-mean-square velocity fluctuations.

Figure 3 shows the root-mean-square (rms) velocity fluctuations normalized by the bulk velocity obtained in our calculations, along with the data of Chung *et al.*[18] and Nouri and Whitelaw.[19] The fluctuating quantities of the experimental data are also rescaled by the normalization process as seen in Fig. 2(a). The calculated fluctuations in the wall-normal [Fig. 3(b)] and azimuthal [Fig. 3(c)] directions are in good qualitative agreement with the experimental data. It is clear from Fig. 3 that the velocity fluctuations increase with increasing N. Furthermore, the fluctuation levels are asymmetric, which can be attributed to the destabilizing effect of the centrifugal forces. The Reynolds shear stresses in the global coordinates are displayed in Fig. 4. Similar to the behavior of the rms velocity fluctuations in Fig. 3, the Reynolds shear stresses increase in strength and become skewed toward the inner wall as N is increased.

B. Flow angle and structure parameter

The differences between the turbulent statistics of a 3DTBL and the corresponding two-dimensional flow can be attributed to the structural changes induced by a moving wall or a mean transverse pressure gradient, to the rotation of the coordinate system aligned with the streamwise vortices, and to the increased mass flow rate.[5] Coordinate rotation effects can be eliminated by introducing an appropriate flow angle. There are several characteristic angles, and those used in the present study are listed below:

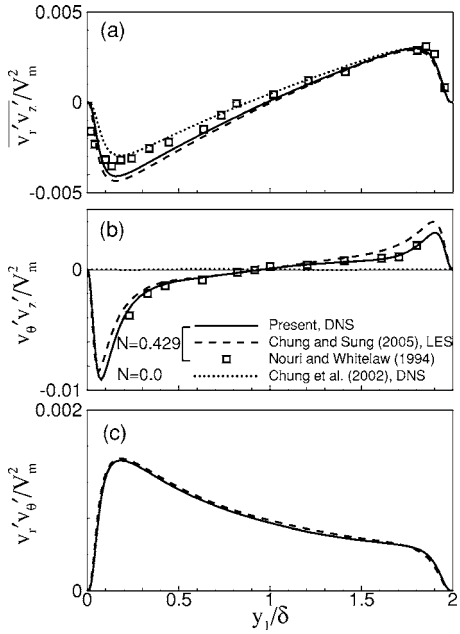

FIG. 4. Distributions of Reynolds shear stresses.

$$\gamma_i = 0.5 \tan^{-1} \frac{2\overline{v_z' v_\theta'}}{\overline{v_z'^2} - \overline{v_\theta'^2}}, \quad \gamma_s = \tan^{-1} \frac{(V_\theta - V_{\theta w})}{V_z},$$
$$\gamma_g = \tan^{-1} \frac{\partial V_\theta / \partial r}{\partial V_z / \partial r}, \quad \gamma_\tau = \tan^{-1} \frac{\overline{v_r' v_\theta'}}{\overline{v_r' v_z'}}, \tag{1}$$

where γ_i, γ_s, γ_g, and γ_τ are the intensity angle, the mean velocity angle, the mean velocity gradient angle, and the Reynolds shear stress angle, respectively. A schematic view of the transformed coordinate systems aligned with γ_τ and γ_i (dashed lines) is shown in Fig. 5. When the coordinates are rotated with the Reynolds shear stress angle, we have $\overline{v_r^{\tau\prime} v_\theta^{\tau\prime}} = 0$. Rotation of the coordinates with the intensity angle maintains $\overline{v_z^{i\prime} v_\theta^{i\prime}} = 0$.

The flow angles γ_i, γ_s, γ_g, and γ_τ for $N=0.429$ are plotted as a function of y^+ in Fig. 6. Among the four angles considered, γ_s and γ_i are the best candidates for minimizing the bulk turning effect on flow structures. Hence, we used the intensity angle γ_i for $N=0.429$ to observe the structural modifications of the turbulent structures, similar to a previous study.[9] It should be noted that the difference between the shear stress angle (γ_τ) and the mean velocity gradient angle (γ_g) is quite large, as has been observed in many previous

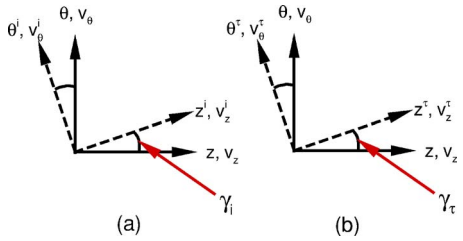

FIG. 5. (Color online) Schematic view of the transformed coordinate systems: (a) for intensity angle and (b) for Reynolds shear stress angle.

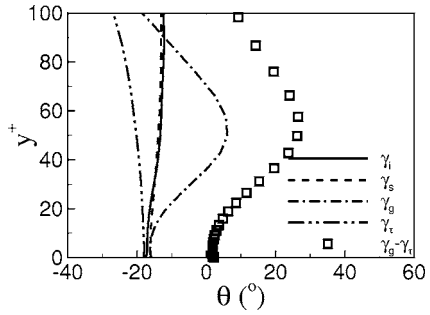

FIG. 6. Profiles of flow angles for $N=0.429$.

studies of 3DTBLs.[4,6,14,16] Because of this difference, scalar eddy-viscosity-type turbulence models for the Reynolds-averaged Navier-Stokes equations are ill suited to simulating flows of this type. If $|\gamma_g - \gamma_\tau|$ is less than 10°, the errors associated with assuming an isotropic eddy viscosity should be less than 3%.[20] In the present study, however, the difference between γ_g and γ_τ reaches values of 27°, indicating that isotropic modeling is inappropriate for the $N=0.429$ system.

To evaluate the efficiency of the eddies in producing turbulent shear stresses for a given amount of turbulence energy, we consider the structure parameter $a_1 = (\overline{v_r' v_z'}^2 + \overline{v_r' v_\theta'}^2)^{0.5}/2k$, as shown in Fig. 7. The value of a_1 increases substantially as N is increased throughout the entire near-wall region. This trend near the wall appears to be due to the increase of the Reynolds shear stress with increasing N, rather than to a diminishing of the turbulent kinetic energy.[1] However, this behavior is the opposite of that found in numerical simulations of rotating pipes and three-dimensional TBLs over a flat plate,[14,21] suggesting that the instability associated with the rotation of the inner wall in a concentric annulus enables more efficient extraction of shear stress from a given amount of turbulent kinetic energy. It is also interesting to note that a_1 is invariant to the intensity angle γ_i, which suggests that the increase in a_1 can be interpreted as a structural change of the turbulent structures. To clarify the increase of the structure parameter on going from $N=0.0$ to 0.429, we carried out various conditional averaging analyses for the Reynolds shear stress $v_r' v_z'$, which are described in the following subsection.

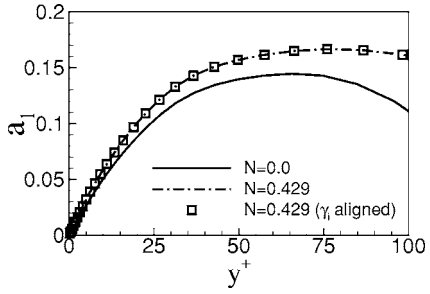

FIG. 7. Distributions of the structure parameter a_1.

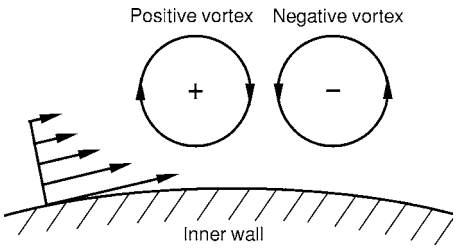

FIG. 8. Schematic diagram of positive and negative vortices near the inner wall.

C. Quadrant/octant analysis and probability density function

In this subsection, we consider various conditional averaging techniques to observe the rotating effect of the inner wall on near-wall turbulent structures. Figure 8 schematically depicts the sign convention for streamwise vortices near the inner wall. The dynamics associated with these vortices are different according to the rotation of the inner wall. In the present study, the sign of a negative vortex is the same as the mean streamwise vorticity. It is well known that the streamwise vortices are the primary contributors to the shear stress in wall-bounded turbulence. Since we are most interested in structural changes of turbulent structures, it would be advantageous to study the three-dimensional effects on the shear-stress-producing events. Quadrant analysis of the Reynolds shear stress provides detailed information on the contributions of various events occurring in the flow to the total turbulence production.[22,23] The analysis divides the Reynolds shear stress into four categories according to the signs of v_z' and v_r'. The first quadrant (Q1), $v_z'>0$ and $v_r'>0$, contains outward motion of high-speed fluid; the second quadrant (Q2), $v_z'<0$ and $v_r'>0$, contains outward motion of low-speed fluid referred to as ejection events; the third quadrant (Q3), $v_z'<0$ and $v_r'<0$, contains inward motion of low-speed fluid; and the fourth quadrant (Q4), $v_z'>0$ and $v_r'<0$, contains an in-rush of high-speed fluid referred to as sweep events. Here, Q1 and Q3 events contribute to the positive Reynolds shear stress (negative production), and Q2 and Q4 events contribute to the negative Reynolds shear stress (positive production).

Figure 9 illustrates the distributions of the Reynolds shear stresses about strong ejections and sweeps at $y^+=10$. Some schematic diagrams of streamwise vortices are added in Fig. 9 for clarity. The conditions for a strong ejection and a strong sweep are as follows:

For a strong ejection, $-v_r'v_z'>2v_{r\,\mathrm{rms}}'\,v_{z\,\mathrm{rms}}'$, and $v_r'>0$;

For a strong sweep, $-v_r'v_z'>2\,v_{r\,\mathrm{rms}}'\,v_{z\,\mathrm{rms}}'$, and $v_r'<0$.

The same criteria are used in Le *et al.*,[9] Littell and Eaton,[11] and Kang *et al.*[13] Here, the frame of reference is aligned with the Reynolds stress angle γ_r. The central peak in each plot, depicting a strong ejection or sweep, is flanked by two secondary peaks generated by the opposite event. Kang *et al.*[13] postulated that these peaks are the signature of the pair of streamwise vortices that generate the strong Reynolds-stress-producing event. The central peak in each plot represents the combined effect of both vortices, while the secondary peaks each correspond to the effect of an individual vortex. Thus, asymmetries in the Reynolds shear stress production by vortices can be discerned by observing the secondary peaks.

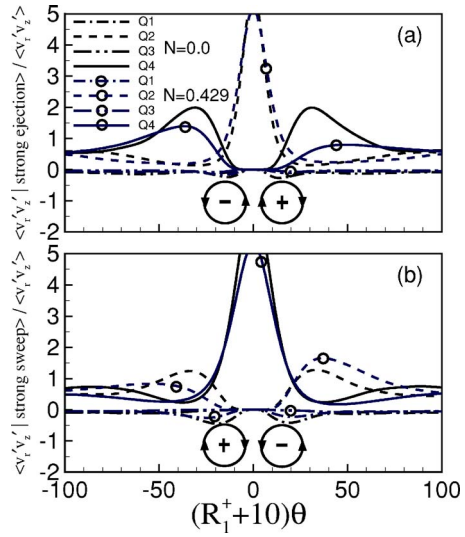

FIG. 9. (Color online) Conditional averages of $v_r'v_z'$ at $y^+=10$: (a) strong ejection and (b) strong sweep.

In contrast to the symmetric secondary peaks for $N=0.0$, the secondary peaks in the plots for the Q2 and Q4 events of the $N=0.429$ system show significant asymmetries in θ (see Fig. 9). It is deduced from the secondary peaks in Fig. 9 that negative (counterclockwise) vortices generate both stronger ejections and sweeps than positive (clockwise) vortices. This suggests that the spanwise flow induced by the rotation of the inner wall augments the negative vortices, but hinders the positive vortices, as observed by Anderson and Eaton.[3]

To see the three-dimensional effect on the symmetry of quasistreamwise vortical structures, we consider the probability density function (pdf) of the streamwise vorticity fluctuations at $y^+=10$ (Fig. 10). Here, the frame of reference is aligned with the intensity angle γ_i for $N=0.429$. In this figure, the streamwise vorticity does not exhibit appreciable asymmetry, suggesting that vortices of each sign are present in equal numbers in the 3DTBL.[9]

Octant analysis of the Reynolds shear stress provides detailed information on the contribution of flow events to the

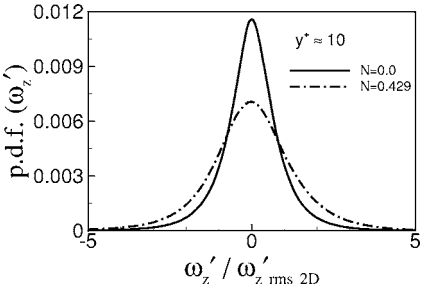

FIG. 10. Pdf of streamwise vorticity at $y^+=10$. Here, the frame of reference is aligned with the intensity angle γ_i for $N=0.429$.

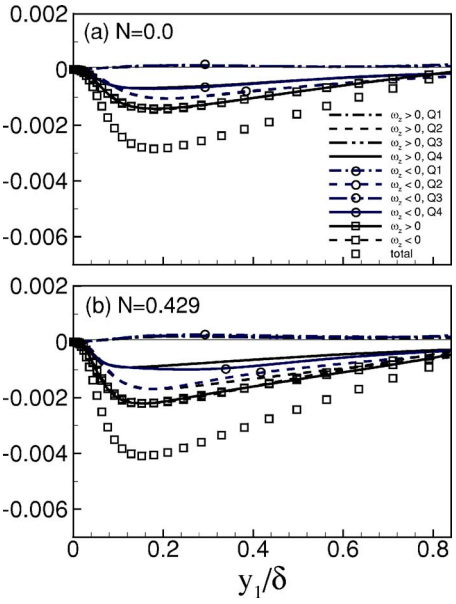

FIG. 11. Reynolds shear stress $v_r'v_z'$ for each octant normalized by V_m^2: (a) $N=0.0$ and (b) $N=0.429$.

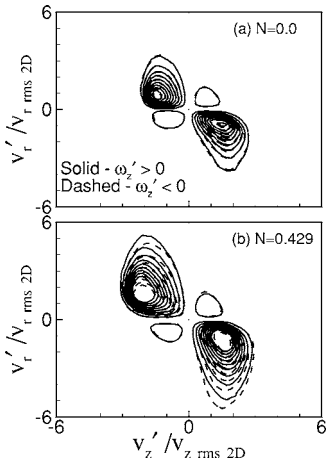

FIG. 12. Weighted joint pdf of v_r' and v_z' at $y^+=10$: (a) $N=0.0$ and (b) $N=0.429$.

production (consumption) of turbulent kinetic energy in three-dimensional turbulent flows.[5] In octant analysis, the Reynolds shear stress is divided into eight categories according to the signs of v_r', v_z', and ω_z'. To explain the three-dimensionality in the strength of each vortex sign, the distribution of the Reynolds shear stress $\overline{v_r'v_z'}$ for each octant is shown in Fig. 11 for $N=0.0$ and 0.429. In this figure, lines marked with a circle correspond to negative values of ω_z'. The frame of reference is aligned with the intensity angle γ_i for $N=0.429$. For $N=0.0$, the flow event of each ω_z' is almost symmetric. It should be noted that, in the region of $0.2 < y_1/\delta < 0.6$, Q4 events with negative ω_z' predominate over those with positive ω_z', whereas Q2 events with positive ω_z' contribute to the Reynolds shear stress to a greater extent than those with negative ω_z'. One remarkable feature of the data in Fig. 11 is that for $N=0.429$, the Reynolds shear stress of positive ω_z' is almost the same as that of negative ω_z'. This phenomenon bears a clear resemblance to the result of the pdf of the streamwise vorticity fluctuations as shown in Fig. 10. Taken together, the octant analysis results indicate that the Reynolds-stress-producing events are significantly affected by three-dimensionality. Moreover, they show that the contribution of Q2 events to the Reynolds shear stress is enhanced for $N=0.429$. This guarantees that the centrifugal force induced by the rotation of the inner wall reinforces the near-wall quasistreamwise vortices.

To better comprehend the modification of the flow structures by the rotation, we examined the weighted joint pdfs of the velocity fluctuations (Fig. 12). Here, the frame of reference is aligned with the intensity angle γ_i for $N=0.429$. The distribution is weighted by $v_r'v_z'$, which reveals how each velocity component contributes to the Reynolds shear stress $\overline{v_r'v_z'}$. Comparison of the $N=0.0$ and $N=0.429$ distributions shows that rotation of the inner cylinder increases the strength of the events in the second (Q2) and fourth (Q4) quadrants. In the nonrotating flow, symmetry dictates that the contributions of positive vortices are the same as those of negative ones. However, Q4 events of negative ω_z' are stronger than those of positive ω_z', whereas Q2 events of positive ω_z' contribute to the Reynolds shear stress to a greater extent than those of negative ω_z'. This is consistent with the results of the octant analysis for Reynolds shear stress $\overline{v_r'v_z'}$, shown in Fig. 11.

Littell and Eaton[11] proposed that rotation-induced cross-flow inhibits strong sweeps from vortices with near-wall spanwise velocities in the same direction as the cross-flow (case 1), but inhibits strong ejections from vortices with spanwise velocities in the opposite direction (case 2). In the present study, "case 1" and "case 2" are negative and positive vortices, respectively, as shown in Fig. 8. However, the pdfs obtained in the present study are not consistent with the behavior described by Littell and Eaton.[11] Rather, the asymmetry of the Reynolds-stress-producing events observed in the present study is closely related to the mechanisms proposed by Sendstad and Moin to describe the behavior in the later period of three-dimensionality.[5] They proposed four mechanisms by which spanwise cross-flow affects particle trajectories in vortical structures. In their work, the 3D flow in a channel was made by the sudden application of spanwise pressure gradient to a 2D channel flow. Sendstad and Moin separated the mechanisms for the initial and later responses of the 2D flow. The initial period was defined as the time when the spanwise boundary layer edge is below $y_{2D}^+ \approx 20$. Within the initial period, the quasistreamwise vortices are not affected by the spanwise boundary layer and the flow is still very similar to a 2D channel flow. After the initial period, the flow becomes more obviously 3D in the sense that the streamwise vortices start to turn in the direction of the mean spanwise pressure gradient. This is called later period. Here we consider the two mechanisms for the later period of three-dimensionality (Mechanisms III and IV in Ref. 5). In Mechanism III, the negative (case 1) vortices are shifted with respect to the wall layer streaks below them, and the negative vortices pump high- rather than low-speed fluid away from the wall. In Mechanism IV, the high-speed fluid swept toward the wall by the positive (case 2) vortices is convected

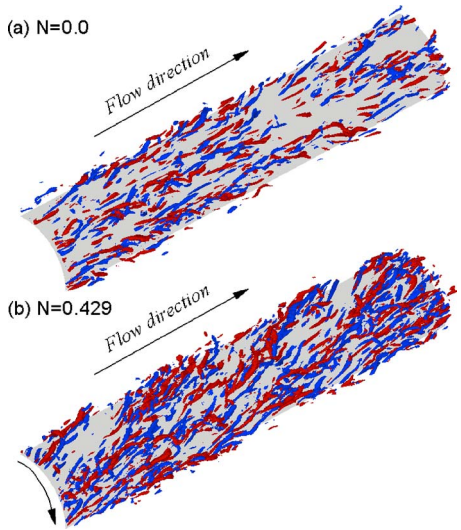

FIG. 13. (Color online) Isosurface plots of $\lambda_2=-0.01$ near the inner wall. Red and blue shading represents positive and negative vortices, respectively.

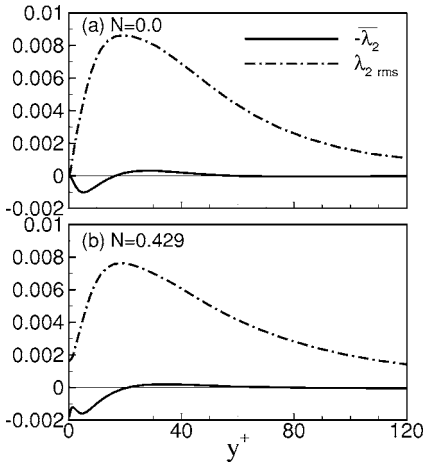

FIG. 14. Profiles of mean and rms of $-\lambda_2$: (a) $N=0.0$ and (b) $N=0.429$.

away from the vortex in the same direction as the spanwise cross-flow. Despite the different mechanisms in generating 3D flows, we observed the similar behaviors of the quasistreamwise vortices to those in Sendstad and Moin.[5]

As will be discussed in Sec. III D, visualizations of the 3DTBLs performed in the present study demonstrate that the asymmetries of the Q2 and Q4 events arise from deformations of the vortical structures. The alterations of the vortical structures by the rotation are consistent with those expected under Mechanisms III and IV of Sendstad and Moin.[5] It should be noted that Sendstad and Moin[5] generated the 3DTBL by a mechanism different from that used in the present study; however, the three-dimensionalities in the present study could be explained by the mechanisms of the later period in Sendstad and Moin[5] since the flow was sufficiently adjusted to the spanwise mean shear in Sendstad and Moin.[5]

D. 3D conditional averaging

Sendstad and Moin[5] proposed four key mechanisms by which the near-wall vortical structures are modified in 3DTBLs. In devising these mechanisms, they assumed that the near-wall vortices are aligned horizontally in the two-dimensional (2D) flow, and respond in a 2D manner to the spanwise shear. Contrary to this assumption, however, a recent study of coherent structures in two dimensional turbulent boundary layers (2DTBLs) indicated that near-wall vortices are generally inclined in the vertical $(y\text{-}z)$ plane and tilted in the horizontal $(x\text{-}z)$ plane.[24] These findings thus indicate that the formation of near-wall turbulent structures is inherently three-dimensional even in 2DTBLs. Hence, it is crucial to investigate 3DTBLs in a 3D manner.

Many experimental studies of turbulent boundary layers have provided evidence that most turbulence production near the wall arises from recurring "bursting" processes in the near-wall region. A number of conditional averaging techniques have been developed to capture these burst events, with the most popular being the Q2 (Quadrant 2)-Q4 (Quadrant 4)[22] and variable-interval time-average [25] eduction schemes. Since these methods are based on the velocity signal, the educed structure can be severely smeared, making accurate analysis of the kinematics and dynamics of coherent structures practically impossible. Clearly, a more appropriate eduction scheme is required for analyzing the detailed features of the underlying vortical structures. To this end, we adopt the vortex identification method of Jeong and Hussain.[26] They defined a vortex as a connected region of negative λ_2, which is the second largest eigenvalue of the tensor $S_{ik}S_{kj}+\Omega_{ik}\Omega_{kj}$, where $S_{ij}\equiv(u_{i,j}+u_{j,i})/2$ is the strain rate and $\Omega_{ij}\equiv(u_{i,j}-u_{j,i})/2$ is the rotation tensor. This definition has been validated for a variety of vortical flows, including both DNS data and analytical solutions.[24,26] Figure 13 shows the isosurfaces of $\lambda_2=-0.01$ near the inner wall. Red and blue shading represent positive and negative vortices, respectively, distinguished by the sign of the axial vorticity. For $N=0.429$, the elongated quasistreamwise vortices are tilted in the direction of the wall shear stress and are more activated than those of $N=0.0$.

Before proceeding further, it is important to identify the preferred location of the vortical structures. To achieve this, we first examine some statistics associated with λ_2. The mean and rms values of λ_2 are displayed in Fig. 14. In the region of $y^+<10$, $\overline{\lambda_2}$ is positive and comparable in magnitude to the rms of λ_2. This indicates that the viscous sublayer contains no vortices, because λ_2 is always positive outside vortex cores. For both $N=0$ and 0.429, the rms value of λ_2 is greatest at $y^+\approx 20$, suggesting the prominence of vortical structures in the buffer region. Note that the rms value of λ_2 at $y^+\approx 20$ for $N=0.0$ is a little higher than that for $N=0.429$ because it is normalized by Q_τ and $\nu(\lambda_2\nu^2/Q_\tau^4)$. In the region $10<y^+<40$, $\overline{\lambda_2}$ is much smaller than the rms of λ_2, indicating substantial cancellation of positive and negative regions of λ_2 in the buffer region. Thus, the rms of λ_2 is better than $\overline{\lambda_2}$ as an indicator of vortical structures. It is interesting to note that the rms of λ_2 at the inner wall for $N=0.429$ seems quite larger than that for $N=0.0$ in Fig. 14. This is due to the relatively large spanwise mean shear at the inner wall for $N=0.429$. The near-wall behavior of λ_2 is not affected by the rotation of the inner wall.

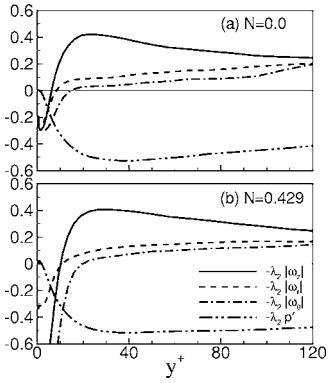

FIG. 15. Cross-correlation of $-\lambda_2$ with $|\omega_z'|$, $|\omega_r'|$, $|\omega_\theta'|$, and pressure fluctuations: (a) $N=0.0$ and (b) $N=0.429$.

The cross-correlations of $-\lambda_2$ with the magnitudes of the fluctuations in the vorticity (i.e., $|\omega_z'|$, $|\omega_r'|$, and $|\omega_\theta'|$) and pressure are shown in Fig. 15 for the $N=0.0$ and 0.429 systems. Here, the frame of reference is aligned with the intensity angle γ_i for $N=0.429$. Near the wall ($10<y^+<40$), the cross-correlation between $-\lambda_2$ and $|\omega_z'|$ is higher than that between $-\lambda_2$ and $|\omega_r'|$ or $|\omega_\theta'|$, suggesting that the structures are aligned almost parallel to the streamwise direction. It is interesting to note that the cross-correlation between $-\lambda_2$ and the pressure fluctuation level is as high as that between $-\lambda_2$ and $|\omega_z'|$, indicating that the coherent structures detected by λ_2 contain regions of low pressure. This result is consistent with the definition of λ_2, which is based on the Hessian of the pressure. The inverse, however, is not true; i.e., not all regions of low pressure are included in the λ_2-based vortex definition. The joint pdfs between pressure fluctuation and ω_z' also support this result.[27]

Motivated by the statistics of λ_2 shown in Figs. 14 and 15, we now consider a fully three-dimensional ensemble average using the λ_2-based identification. Our eduction scheme consists of three basic steps. (I) Detect quasistreamwise vortical structures using the λ_2 definition, where the sign of the vortex is given by ω_z' and the reference frame for ω_z' is aligned with the intensity angle γ_i for $N=0.429$. The choice of the y position ($y^+=20$) for the detection of vortices is based on the rms values of λ_2 which show a peak located at $y^+=20$ (see Fig. 14). To capture the individual vortices effectively, the threshold of the streamwise vorticity is set to three times the rms value of the streamwise vorticity for $N=0.0$ (i.e., $|\omega_z'|>3\omega_{z\,\mathrm{rms,2D}}'$). (II) Ensemble average the accepted structures with the same sign of rotation by aligning the midpoints of their streamwise lengths. (III) Shift the alignment point to maximize the cross-correlation between the individual structures and the ensemble-averaged field. The cross-correlations were computed over three-dimensional windows of $300\times100\times200$ and $400\times100\times300$ wall units in x^+, y^+, and z^+ for $N=0.0$ and $N=0.429$, respectively. Here, x^+, $y^+=r^+\cos\theta-R_1^+$ and $z^+=r^+\sin\Delta\theta$ denote the spatial coordinates in the streamwise, wall-normal, and spanwise directions, respectively. The ensemble averages were based on databases consisting of 28 instantaneous flow fields for both N. The individual flow fields were separated in time by 30 wall time units (ν/Q_τ^2). The fractions of the total examined area covered by the coherent structures (number of realizations times the cross-sectional area/total area) were about 15% for both N.

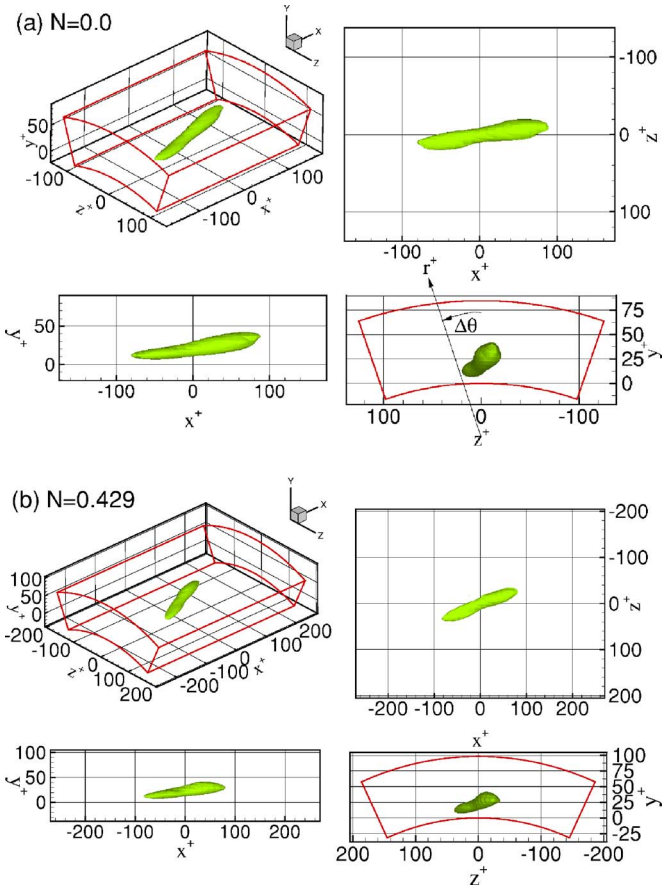

FIG. 16. (Color online) Isosurface plots of the ensemble-averaged positive vortices: (a) $N=0.0$ and (b) $N=0.429$.

Isosurfaces of λ_2 for the educed vortices with positive and negative ω_z' are illustrated in Figs. 16 and 17, respectively. In the nonrotating case ($N=0.0$), the inclination angles in the vertical plane are about 9° for the positive and negative vortices, respectively, and both types of vortex exhibit a tilting angle of about ±6° in the horizontal plane. These angles are very similar to those reported by Jeong *et al.*[24] for coherent structures (an inclination angle of about 9° in the vertical plane and a tilting angle of ±4° in the horizontal plane). The inclination and tilting angles are calculated from the positions of the head and tail of a vortex. We detected the head and tail of a vortex using an enlarged view. When the inner wall is rotated ($N=0.429$), however, the inclination angles for positive and negative vortices change to about 8° and 13°, respectively. The higher inclination angle of the negative vortex compared to the positive one in the $N=0.429$ system is attributed to the centrifugal force induced by the rotation of the inner wall. Since the negative vortex is lifted up away from the wall, it can be strengthened by a vortex stretching mechanism. This phenomenon is closely linked to the increase in the structure parameter a_1 with moving away from the wall (see Fig. 7). Rotation of the inner wall directly affects the upstream ends of the vortices, and causes the tilting angles in the negative z direction to in-

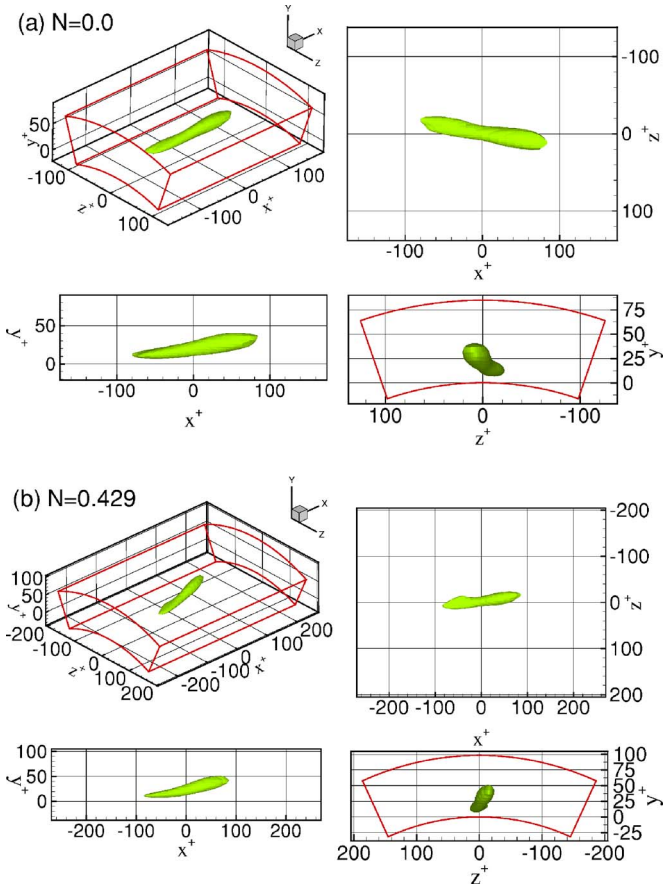

FIG. 17. (Color online) Isosurface plots of the ensemble-averaged negative vortices: (a) $N=0.0$ and (b) $N=0.429$.

crease. The tilting angles for $N=0.429$ are about $-20°$ for the positive vortex and $-8°$ for the negative vortex. Note that the educed vortices have streamwise extents of 200 wall units and diameters of 25 wall units for all cases, consistent with the dimensions reported in a previous study.[24]

To further explore the 3D effects on the coherent structures, we examined contour plots of the Reynolds shear stresses and vector plots near the ensemble-averaged vortices at three x^+ positions (Figs. 18–20). In these figures, thick (black) and red contours denote the centers of educed vortices and the Reynolds shear stresses, respectively. At $x^+=0.0$ (Fig. 18), the ejection motion near the vortices occurs at a higher position than the sweep motion, as indicated by a previous study.[24] It is notable that the enhanced ejections for $N=0.429$ [Figs. 18(c) and 18(d)] are apparent near the vortices at $x^+=0.0$. This is due to the upward motion induced by the centrifugal force, as mentioned above. In addition, the Q4 event near the positive vortex is weaker than that near the negative vortex, consistent with the results of the octant analysis for the Reynolds shear stress $v_r'v_z'$. The high-speed fluid swept toward the wall by the positive vortex is partially convected away from the vortex in the same direction as the spanwise cross-flow, as discussed in Sec. III C (Mechanism IV of Sendstad and Moin[5]). This deformation of vortical motion is more apparent at $x^+=70.0$ [Fig. 19(c)]. At the upstream end of the negative vortex for $N=0.429$ [Fig. 20(d)], the negative vortex is shifted with respect to the wall layer

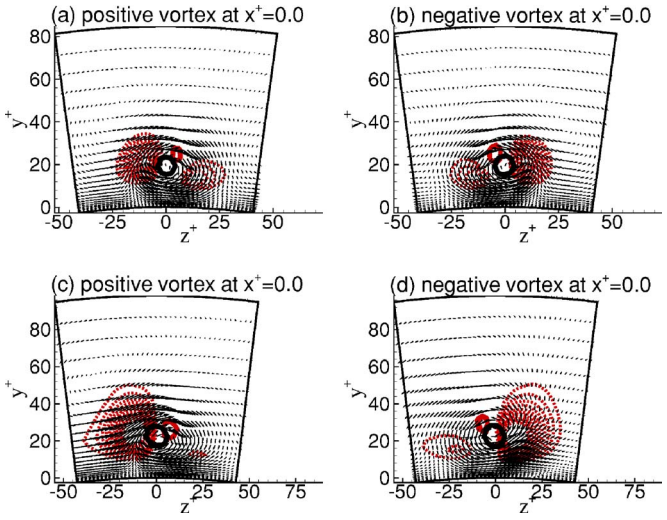

FIG. 18. (Color online) Contours of Reynolds shear stress and vector plots near coherent vortices in the r-θ plane at $x^+=0.0$: (a) and (b) $N=0.0$; (c) and (d) $N=0.429$. In Figs. 18–20, thick (black) and red contours denote the centers of educed vortices and the Reynolds shear stresses, respectively.

streaks below it. The negative vortex pumps high- rather than low-speed fluid away from the wall (Mechanism III of Sendstad and Moin[5]). Thus, the educed vortices confirm that the Q4 event of the negative vortex is stronger than that of the positive one, while the Q2 event of the negative vortex is weaker than that of the positive one, as shown in the joint pdf analysis of the velocity fluctuations.

Another notable feature clearly revealed in the visualization study of the coherent vortices is that the negative vortex is lifted by the rotation of the wall [Fig. 19(d)]. This implies that the wall rotation reinforces the negative vortex through a vortex stretching mechanism. It can also be deduced that the lifted vortex is less affected by viscous dissipation than the other vortices. Figure 21 shows schematic three-dimensional views of vortices for rotating cases. The centrifugal force by the rotating inner wall is exerted mainly on the upper right

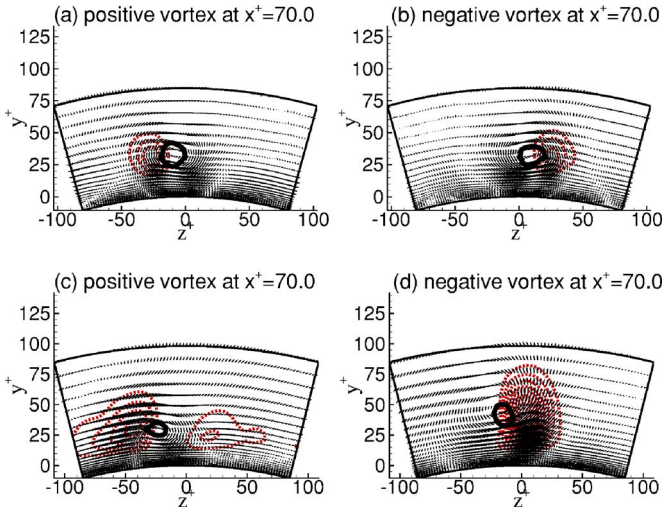

FIG. 19. (Color online) Contours of Reynolds shear stress and vector plots near coherent vortices in the r-θ plane at $x^+=70.0$: (a) and (b) $N=0.0$; (c) and (d) $N=0.429$.

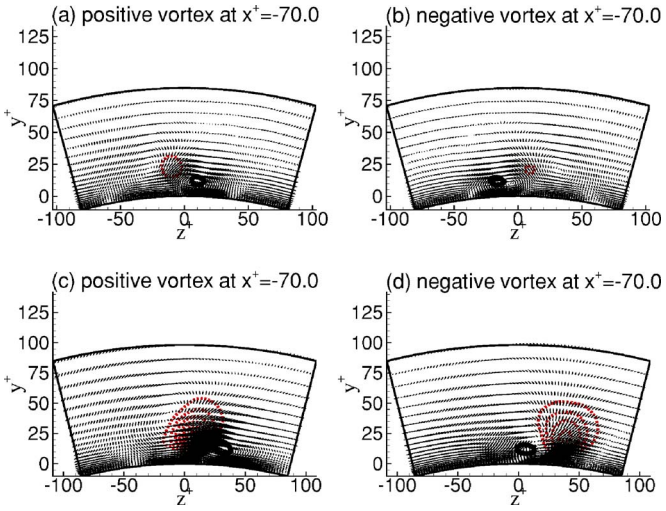

FIG. 20. (Color online) Contours of Reynolds shear stress and vector plots near coherent vortices in the r-θ plane at $x^+=-70.0$: (a) and (b) $N=0.0$; (c) and (d) $N=0.429$.

side of the positive vortex (see the front view of positive vortex). Thus, the rotation enhances the Q2 event near the positive vortex. The negative vortex is lifted and exposed to the high speed region of the fluid by the rotation. Therefore, the negative vortex can be stretched and the strong Q2 and Q4 events can be observed near the negative vortex. Littell and Eaton[11] assumed that the three-dimensionality in the Reynolds-stress-producing events is connected to the reduction of the Reynolds shear stress $\overline{v_r' v_z'}$. Figures 19(c) and 19(d) show that the cross-flow hinders strong sweeps from the negative vortex, while preventing strong ejections from the positive one. However, our observation that the vortical structures in 3DTBLs are more activated than those in 2DTBLs cannot be explained by the mechanism proposed by Littell and Eaton.[11] Our results clearly show that the features of a 3DTBL depend on the flow configuration, especially the transverse curvature. Further in-depth investigations are therefore needed to clarify the dependence of the turbulent structure on the curvature.

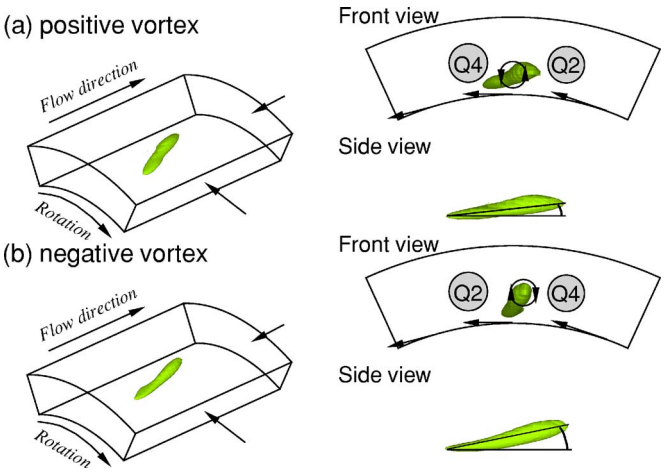

FIG. 21. (Color online) Schematic 3D views of vortices near the inner wall for $N=0.429$.

IV. SUMMARY AND CONCLUSIONS

Direct numerical simulations of fluid flow through a concentric annulus with a rotating inner wall were performed at $\mathrm{Re}_{Dh}=8900$. To elucidate the modifications of the near-wall turbulent structure induced by rotation of the inner wall, we compared data obtained at rotation rates of $N=0.0$ and 0.429 for a system with a radius ratio (R^*) of 0.5. We found that among the four characteristic flow angles, the mean velocity angle γ_s and the intensity angle γ_i were the best candidates for minimizing the bulk turning effect on flow structures. Comparison of the values of the structure parameter a_1 for the systems with and without inner wall rotation indicated that the production of turbulent shear stress for a given amount of turbulent kinetic energy is more efficient in the 3DTBL of the concentric annulus with a rotating inner cylinder. Conditional quadrant/octant analysis and the pdfs of the velocity fluctuations revealed distinctive features of the 3DTBL. In particular, it was apparent that the Reynolds-stress-producing events are significantly affected by three-dimensionality. The present results were consistent with the two mechanisms in the later period of three-dimensionality proposed by Sendstad and Moin.[5] Finally, coherent structures near the inner wall were detected by $-\lambda_2$ vortex identification to give the detailed information on the activated near-wall turbulent structures. The ensemble-averaging of the educed coherent vortices revealed that enhanced ejections near the vortices are primarily responsible for the augmented turbulent structures. The alteration of the turbulent structures was attributed to the centrifugal force arising from rotation of the inner wall. The assumption of Littell and Eaton[11] on the cause of the altered turbulent structures in 3DTBLs was invalid in the present study. Taken together, the present results showed that the 3DTBL in a rotating concentric annulus has features different from those observed in other types of 3DTBL due to the transverse curvature.

[1] S. Y. Chung and H. J. Sung, "Large-eddy simulation of turbulent flow in a concentric annulus with rotation of an inner cylinder," Int. J. Heat Fluid Flow **26**, 191 (2005).
[2] P. Bradshaw and N. S. Pontikos, "Measurements in the turbulent boundary layer on an 'infinite' swept wing," J. Fluid Mech. **159**, 105 (1985).
[3] S. C. Anderson and J. K. Eaton, "Reynolds stress development in a pressure driven three-dimensional turbulent boundary layer," J. Fluid Mech. **202**, 263 (1989).
[4] P. Moin, T. H. Shih, D. Driver, and N. N. Mansour, "Direct numerical simulation of a three-dimensional turbulent boundary layer," Phys. Fluids A **2**, 1846 (1990).
[5] O. Sendstad and P. Moin, "The near wall mechanics of three-dimensional turbulent boundary layers," Report TF-57, Thermosciences Division, Department of Mechanical Engineering, Stanford University, 1992.
[6] W. R. Schwarz and P. Bradshaw, "Turbulence structural changes for a three-dimensional turbulent boundary layer in a 30° degree bend," J. Fluid Mech. **272**, 183 (1994).
[7] G. N. Coleman, J. Kim, and A. T. Le, "A numerical study of three-dimensional wall-bounded flows," Int. J. Heat Fluid Flow **17**, 333 (1996).
[8] G. N. Coleman, J. Kim, and P. R. Spalart, "A numerical study of strained three-dimensional wall-bounded turbulence," J. Fluid Mech. **416**, 75 (2000).
[9] A. T. Le, G. N. Coleman, and J. Kim, "Near-wall turbulence structures in three-dimensional boundary layers," Int. J. Heat Fluid Flow **21**, 480 (2000).
[10] R. P. Lohmann, "The response of a developed turbulent boundary layer to local transverse surface motion," J. Fluids Eng. **98**, 354 (1976).
[11] H. S. Littell and J. K. Eaton, "Turbulence characteristics of the boundary-

layer on a rotating-disk," J. Fluid Mech. **266**, 175 (1994).
[12]C. Chiang and J. K. Eaton, "An experimental study of the effects of three-dimensionality on the near wall turbulence structures using flow visualization," Exp. Fluids **20**, 266 (1996).
[13]H. S. Kang, H. Choi, and J. Y. Yoo, "On the modification of the near-wall coherent structure in a three-dimensional turbulent boundary layer on a free rotating disk," Phys. Fluids **10**, 2315 (1998).
[14]C. Kannepalli and U. Piomelli, "Large-eddy simulation of a three-dimensional shear-driven turbulent boundary layer," J. Fluid Mech. **423**, 175 (2000).
[15]X. Wu and K. D. Squires, "Prediction and investigation of the turbulent flow over a rotating disk," J. Fluid Mech. **418**, 231 (2000).
[16]M. Lygren and H. I. Andersson, "Turbulent flow between a rotating and a stationary disk," J. Fluid Mech. **426**, 297 (2001).
[17]K. Kim, S.-J. Baek, and H. J. Sung, "An implicit velocity decoupling procedure for the incompressible Navier-Stokes equations," Int. J. Numer. Methods Fluids **38**, 125 (2002).
[18]S. Y. Chung, G. H. Rhee, and H. J. Sung, "Direct numerical simulation of turbulent concentric annular pipe flow. Part 1: Flow field," Int. J. Heat Fluid Flow **23**, 426 (2002).
[19]J. M. Nouri and J. H. Whitelaw, "Flow of Newtonian and non-Newtonian fluids in a concentric annulus with rotation of the inner cylinder," J. Fluids Eng. **116**, 821 (1994).
[20]J. P. Johnston and K. A. Flack, "Review—Advances in three-dimensional wall-bounded flows," J. Fluids Eng. **118**, 219 (1996).
[21]P. Orlandi and M. Fatica, "Direct simulations of turbulent flow in a pipe rotating about its axis," J. Fluid Mech. **343**, 43 (1997).
[22]W. W. Willmarth and S. S. Lu, "Structure of the Reynolds stress near the wall," J. Fluid Mech. **55**, 65 (1972).
[23]R. S. Brodkey, J. M. Wallace, and H. Eckelmann, "Some properties of truncated turbulence signals in bounded shear flows," J. Fluid Mech. **63**, 209 (1974).
[24]J. Jeong, F. Hussain, W. Schoppa, and J. Kim, "Coherent structures near the wall in a turbulent channel flow," J. Fluid Mech. **332**, 185 (1997).
[25]R. F. Blackwelder and R. E. Kaplan, "On the wall structure of the turbulent boundary layer," J. Fluid Mech. **76**, 89 (1976).
[26]J. Jeong and F. Hussain, "On the identification of a vortex," J. Fluid Mech. **285**, 69 (1995).
[27]J. Kim, "On the structure of pressure fluctuations in simulated turbulent channel flow," J. Fluid Mech. **205**, 421 (1989).